



LAWRENCE
LIVERMORE
NATIONAL
LABORATORY

The Effects of Viscosity and Mass Diffusion in Hydrodynamically Unstable Plasma Flows

H. F. Robey

November 12, 2003

Physics of Plasmas

This document was prepared as an account of work sponsored by an agency of the United States Government. Neither the United States Government nor the University of California nor any of their employees, makes any warranty, express or implied, or assumes any legal liability or responsibility for the accuracy, completeness, or usefulness of any information, apparatus, product, or process disclosed, or represents that its use would not infringe privately owned rights. Reference herein to any specific commercial product, process, or service by trade name, trademark, manufacturer, or otherwise, does not necessarily constitute or imply its endorsement, recommendation, or favoring by the United States Government or the University of California. The views and opinions of authors expressed herein do not necessarily state or reflect those of the United States Government or the University of California, and shall not be used for advertising or product endorsement purposes.

The effects of viscosity and mass diffusion in
hydrodynamically unstable plasma flows

H. F. Robey

Lawrence Livermore National Laboratory

Livermore, California 94550

Prepared for submission to

Physics of Plasmas

November 12, 2003

ABSTRACT

Hydrodynamically unstable plasma flows driven by intense laser radiation are described in which an interface between two materials of dissimilar densities is subjected to a very strong shock and then decelerated over a longer time scale. Pre-imposed perturbations on this interface are unstable to a combination of the Richtmyer-Meshkov (RM) and Rayleigh-Taylor (RT) instabilities. Overall target dimensions for these experiments are of the order of 1 mm, and length scales of the unstable perturbations of interest can be as small as a few microns. At such small spatial scales, the effects of dissipative processes such as viscosity, thermal conductivity, and mass diffusion begin to affect instability growth rates.

In this paper, estimates are presented of the spatial scale at which viscosity and mass diffusion begin to affect the growth of a perturbation due to the RM and RT instabilities. Time dependent values for the plasma kinematic viscosity and interfacial binary mass diffusivity are estimated for the conditions occurring in laser-driven instability experiments recently conducted on the Omega laser. These are used together with several models in the literature for estimating the reduction in the growth rate dispersion curves of the Rayleigh-Taylor and Richtmyer-Meshkov instabilities due to the presence of these small-scale dissipative effects.

I. INTRODUCTION

Hydrodynamically unstable flows driven by intense laser radiation are described in which the interface between two materials of dissimilar densities is first subjected to a very strong shock and then decelerated over a longer time scale. Perturbations on this interface are unstable to a combination of the Richtmyer-Meshkov (RM) [1-2] and Rayleigh-Taylor (RT) [3-4] instabilities. These experiments serve as a testbed for the study of similar high Mach number, high Reynolds number instability-driven systems that occur on very different spatial scales.

A large-scale application of this testbed arises in the astrophysical problem of core-collapse supernovae. In a supernova explosion, the He-H interface of the progenitor star undergoes a very similar acceleration history, with the interface being impulsively accelerated by a very strong shock and then subsequently decelerated by the surrounding lower density hydrogen envelope [5-9]. In this case, length scales are vastly larger than those occurring in the laser-driven laboratory experiment. Care must be taken to insure that the same physics is governing the hydrodynamic evolution in these two cases. Specifically, we are concerned in this paper with the onset of dissipative effects, which occur at small spatial scale. Since the laboratory experiment scale is so small compared with the astrophysical application, we need to assess whether effects of viscosity, thermal conductivity, and mass diffusion change the character of the instability evolution from that which would occur in a system of much larger scale.

A second application in which small-scale dissipative effects have been shown to be of importance occurs in the implosion of double-shell ICF ignition targets [10-12]. In this case, the specific acceleration history differs for each unstable interface within the target, but as shown in ref. [10] both the RM and RT instabilities again play an important role. Perturbation length scales in this case arise from the surface roughness spectrum initially present on the various concentric shells within the target. As shown in ref. [10], the short

wavelength portion of this spectrum is clearly affected by small-scale dissipative effects. The estimation of the spatial scale at which instability evolution departs from the classical behavior is therefore very important, as it sets the resolution required in numerical simulations to accurately predict the impact of mixing on the capsule performance. For NIF-scale ignition capsules, the Reynolds number is shown to be large ($Re \sim 10^5$) and instability growth near the time of minimum volume is predicted to be approaching a turbulent state. The full numerical simulation of such a high Reynolds number flow including all scales of motion is beyond the present state of the art. Experimental verification using a similar instability-driven system occurring at a larger, more diagnosable scale would therefore be quite useful in verifying the predictions of numerical simulations.

The small-scale processes that can affect the perturbation growth are due to the transport of momentum (viscosity), heat (thermal conductivity), and mass (diffusion). In this paper, we will focus only on two of these, viscosity and mass diffusion. The reason for this is two-fold. Whereas viscosity and mass diffusion provide a purely stabilizing force at short perturbation wavelengths, the effect of thermal conductivity is more complicated. As shown by Ryutov [13], the effect of thermal conductivity on the RT instability can be either stabilizing or destabilizing, depending on the molecular weight of the interface materials.

A second reason for focusing on viscosity and diffusion is that these two mechanisms are not included in numerical simulations [5-12] of high energy density flows, whereas thermal conductivity is explicitly included in all of these simulations. As experiments and simulations move toward the study of shorter wavelength perturbations, these dissipative effects will introduce a source of error in the numerical simulations. The goal of this paper is to estimate the scale at which this occurs in both the Rayleigh-Taylor and Richtmyer-Meshkov instabilities.

II. EXPERIMENTAL SETUP AND RESULTS

A. Experimental Setup

The experiments to be considered are conducted on the Omega Laser at the Laboratory for Laser Energetics (LLE), University of Rochester [14-16]. Figure 1(a) shows a photograph of a typical target that is used in the experiments. The target consists of a cylindrical shock-tube package containing the interface of interest mounted together with a thin metal backlighter foil, which is used to generate x-rays for diagnosing the target. The target materials are mounted within a Beryllium shock tube with an outer diameter (OD) of 1100 μm and an inner diameter (ID) of 800 μm . The shock-tube is used to improve the planarity of the experiment by decreasing the lateral expansion of the target materials. Beryllium is used for the shock-tube material, since it is highly transparent to the diagnostic x-rays. The length of the shock tube is typically of order 2 mm long.

Figure 1(b) shows a two-dimensional slice through the center of the target. The target consists of a 150 μm thick polyimide layer ($\rho = 1.41 \text{ g/cm}^3$), with the remainder of the target filled with a low-density carbonized resorcinol formaldehyde (CRF) foam ($\rho = 0.1 \text{ g/cm}^3$). Embedded within the polyimide layer is a radiographically opaque tracer strip of 4.3% brominated polystyrene (CH) as shown at the bottom of Figure 1(b) in an end-on view of the target. This tracer layer measures 75 μm in the direction along the Be tube, and is 200 μm wide in the transverse or diagnostic line-of-sight direction. The density of the CH(Br) layer ($\rho = 1.42 \text{ g/cm}^3$) is nearly identical to that of the surrounding polyimide. When viewed in side-illuminated radiography, most of the contrast comes from this opaque tracer layer, allowing visualization of the interfacial structure over only the central 200 μm of the target. This helps to eliminate wall effects that are inherent in such an integrated line-of-sight diagnostic [17].

The strong shock conditions of interest are achieved by directing 10 beams with a nominal measured energy of 500 J / beam at a laser wavelength of 0.351 μm onto the target. Each beam has a super-Gaussian spatial intensity profile defined as $I / I_0 = \exp [-(r / 412\mu\text{m})]^{4.7}$. The combined spatial profile of all drive beams also follows this profile, with $I_0 = 9 \times 10^{14} \text{ W/cm}^2$. The intensity is reasonably constant over a central diameter of 600 μm ,

and falls off by about 10% by $800 \mu\text{m}$. For all experiments, the temporal pulse is nominally flat with a temporal duration of 1 ns.

B. Experimental Results

The basic target geometry shown in Figure 1 has been used to study the evolution of a wide range of perturbations [9]. For all perturbation geometries considered, the underlying acceleration history of the interface is the same. The deposition of laser energy at $t = 0$ generates a strong shock wave, which passes through the interface at $t = 3$ ns impulsively accelerating it. The interface then gradually decelerates over the remainder of the experiment. The acceleration / deceleration history of the mean interface is shown in Figure 2(a). This acceleration history is obtained from a numerical simulation using a one-dimensional radiation-hydrodynamics code HYADES [18]. More complete details of the simulations including time histories of the pressure, density, temperature, and degree of ionization are given in [19].

The acceleration history shown in Figure 2(a) initiates instability growth of perturbations imposed on the interface due to a combination of both the Richtmyer-Meshkov and Rayleigh-Taylor instabilities. The amount of RM growth is significant early in time, but quickly becomes small in comparison to the subsequent RT growth as the interface is decelerated. Both instability mechanisms depend on the Atwood number of the interface, which is plotted in Figure 2(b). Even though the density on either side of the interface is monotonically decreasing following shock passage through the interface [19], the Atwood number remains relatively constant throughout the experiment at $A = 0.55$.

In reference [19], this experiment geometry was used to study the growth of a pre-imposed perturbation consisting of a single sinusoidal component. In this paper, we will focus on perturbations of more complicated modal content, as the goal is to study the effect of dissipative effects on short wavelength perturbations. Figure 3 shows examples of experimental radiographs obtained at $t = 13$ ns, using three different initial interface

perturbations. In all cases, the instability evolution was diagnosed with x-rays generated by directing an additional 7 Omega beams onto a $2.5 \times 2.5 \text{ mm}^2$ by $12 \mu\text{m}$ thick titanium backlighter foil located 4 mm from the center of the target as shown in Figure 1(a). These beams, driven by a separate oscillator, were delayed in time relative to the drive beams. The contrast generated by differential absorption of the backlighter x-rays by the target materials is then imaged with a gated framing camera [20], producing the radiographs of Figure 3.

Figure 3(a) shows the structure resulting from an initially imposed single sinusoidal component with wavelength $\lambda = 50 \mu\text{m}$ and initial amplitude $a_0 = 2.5 \mu\text{m}$. The perturbation is clearly seen due to the high opacity of the radiographic tracer layer (Br) embedded in the interface. The transmitted shock is seen as well due to the difference in optical depth of the shocked vs. the un-shocked foam. A reference grid consisting of $15 \mu\text{m}$ Au wires with a period of $63 \mu\text{m}$ was used to determine the mean interface location and the peak-to-valley amplitude of the interfacial perturbation. Figure 3(b) shows the structure arising from the same acceleration history, but with an initial perturbation consisting of two sinusoidal components with wavelengths, $\lambda_1 = 60 \mu\text{m}$ and $\lambda_2 = 40 \mu\text{m}$ and corresponding initial amplitudes of $a_1 = 0.75 \mu\text{m}$ and $a_2 = 0.5 \mu\text{m}$, respectively. The resulting structure at $t = 13 \text{ ns}$ is somewhat more complicated than that for the single mode perturbation. Figure 3(c) shows the corresponding interfacial structure arising from an initial perturbation with eight sinusoidal modes. The wavelengths are given by $\lambda_i = (180 \mu\text{m}) / i = (180, 90, 60, 45, 36, 30, 25.7, 22.5 \mu\text{m})$. The corresponding amplitudes of each component were randomly generated to give a maximum perturbation amplitude of $2.5 \mu\text{m}$, the same as for the other two perturbations shown in Figure 3. The interfacial structure shown in Figure 3(c) is considerably more complicated than that arising from the single or two-mode perturbations.

In each case shown in Figure 3, the perturbation is visually seen to be non-linear, with a clearly asymmetric spike-bubble structure as well as vortical roll-up evident at the spike tips. In reference [19], it was shown that the single-mode perturbation enters the non-linear regime within the first few nanoseconds following shock passage through the

interface. The onset of non-linearity in the perturbation development gives rise to additional modal components in the perturbation spectrum [21, 22]. Structure will arise at both longer and shorter wavenumbers given by $k_i - k_j$ and $k_i + k_j$, respectively, where modes (i, j) are any of the pre-imposed modes of the initial perturbation. In the two-mode case, for example, additional perturbations will be generated with shorter wavelengths of 20, 24, and 30 μm and a longer wavelength of 120 μm . This longer wavelength component is clearly seen in Figure 2(b) as the spacing between the longer, non-bifurcated spikes. For the eight-mode case, the spectrum resulting from non-linear interaction is more extensive. Since we are interested here in the short wavelength behavior, Table 1 lists the modes resulting from the non-linear interaction of $k_i + k_j$.

Table 1

λ (μm)	$k_{nl} = k_i + k_j$ (rad/ μm)
11.25	0.56
12.00	0.52
12.86	0.49
13.85	0.45
15.00	0.42
16.36	0.38
18.00	0.35
20.00	0.31

In addition to the perturbations shown in Figure 3, the same experiment geometry has also been used to study the evolution of other initial perturbation spectra. In reference [23], for example, an extensive discussion is presented for the case of the interaction of two modal components with widely spaced initial wavelengths, $\lambda_1 = 50 \mu\text{m}$ and $\lambda_2 = 5 \mu\text{m}$. The corresponding initial amplitudes are $a_1 = 2.5 \mu\text{m}$ and $a_2 = 0.25 \mu\text{m}$, respectively. The non-linear interaction of these modes produces the additional shorter wavelengths components given in Table 2.

Table 2

λ (μm)	$k_{nl} = k_i + k_j$ (rad/ μm)
2.5	2.51
4.55	1.38
5.56	1.13
25	0.25

In the following sections, the effect of viscosity and mass diffusion on the RM and RT growth of these perturbations subjected to the acceleration history of Figure 2 will be quantified. The goal is to obtain an estimate of the spatial scale at which these dissipative processes begin to significantly alter the evolution of the perturbation growth.

III. ESTIMATION OF DISSIPATIVE TRANSPORT PARAMETERS

A. Plasma kinematic viscosity

In this Section, a brief discussion of the small-scale dissipative transport properties is given for the experiment of interest. A more complete discussion is found in [19]. The plasma kinematic viscosity is estimated by two methods. The simplest formula for the estimation of the viscosity of a plasma is that given by Braginskii [24], which is applicable to the low density, high temperature plasma state where ionic coupling is weak. The coupling is determined by the plasma parameter $\Gamma = Z^2 e^2 / (k_B T \lambda_i)$, where ($Z \cdot e$) is the ionic charge and $\lambda_i = (3/4\pi N_i)^{1/3}$ is the average inter-ionic distance (N_i is the ion number density in cm^{-3}). Γ is therefore a measure of the ratio of potential to kinetic energy of the plasma.

For $\Gamma \ll 1$, the plasma ions are weakly coupled, and the formula of Braginskii for the kinematic viscosity is given as

$$\nu_i = 3.3 \times 10^{-5} \frac{\sqrt{A} T^{5/2}}{\ln(\Lambda) Z^4 \rho_i} \quad (1)$$

Here, ν is the kinematic viscosity in cm^2/s , T is the ion temperature measured in eV, ρ is the density in g/cm^3 , A and Z are the atomic weight and number, and $\ln(\Lambda)$ is the Coulomb logarithm, which is again a function of temperature and degree of ionization. For numerical evaluation of the kinematic viscosity, we use the Coulomb logarithm definition given in the NRL Plasma Formulary [25].

For dense plasma conditions or for conditions where mixing between two ionic species is involved, we also use the more extensive viscosity model of Clerouin et al. [26], which is applicable over a wider range of temperatures and densities than the Braginskii model. For this model, the kinematic viscosity is given by

$$\nu \text{ (cm}^2/\text{s)} = 6.55 \times 10^{-10} Z_{\text{eff}} m_i^{1/2} n_i^{5/6} \begin{cases} 1.1 \Gamma_{\text{eff}}^{-1.895}, & \Gamma_{\text{eff}} < 2 \\ \lambda I_1 + \frac{(1 + \lambda I_2)^2}{\lambda I_3}, & 2 < \Gamma_{\text{eff}} < 160 \end{cases} \quad (2)$$

where the parameter λ and fits to the integrals I are given by

$$\begin{aligned} \lambda &= \frac{4\pi}{3} (3\Gamma_{\text{eff}})^{3/2} \\ I_1 &= (180\pi^{3/2} \Gamma_{\text{eff}})^{-1} \\ I_2 &= (1/60\pi^2) (0.49 - 2.23 \Gamma_{\text{eff}}^{-1/3}) \\ I_3 &= (1/10\pi^{3/2}) (2.41 \Gamma_{\text{eff}}^{1/9}) \end{aligned} \quad (3)$$

Here $Z_{\text{eff}} = x_1 Z_1 + x_2 Z_2$ is the number-density-weighted average charge for a binary ionic mixture of two species with number densities x_1 and x_2 . The effective plasma coupling parameter for this mixture is

$$\Gamma_{\text{eff}} = \frac{e^2 \overline{Z^{1/3}} \overline{Z^{5/3}}}{a k_B T}, \quad \overline{Z^{5/3}} = x_1 Z_1^{5/3} + x_2 Z_2^{5/3} \quad (4)$$

where a is the mean ionic radius, and k_B is the Boltzmann constant. This model was developed by performing molecular dynamics simulations in the dense plasma regime and extrapolating the results to the dilute plasma regime ($\Gamma_{\text{eff}} \ll 1$). The resulting model gives results in good agreement with the model of Braginskii in the low-density regime where both are applicable, as shown in [19].

From the one-dimensional numerical simulation of the experiment [19], the plasma coupling parameter Γ was calculated. This is plotted in Figure 4(a). Two curves are shown, one based on the material properties of the high-density material on one side of the interface, and one based on the low-density material properties. After passage of the shock, the plasma parameter is seen to be in the “uncomfortable” range close to one, i.e. neither in the weakly couple regime where kinetic theory is valid ($\Gamma \ll 1$) nor the very strongly coupled regime ($\Gamma \gg 1$).

The kinematic viscosity, calculated using both the Braginskii formula (dashed curves) as well as that of Clerouin et al. (solid curves), is plotted in Figure 4(b). Again the viscosity is plotted using the “pure” material properties on both sides of the interface. After passage of the shock, ν remains reasonably constant at approximately 0.1-0.2 cm²/s for the denser polyimide and 0.04-0.05 cm²/s for the carbon foam. In reality, there will be some degree of atomic scale mixing occurring at the interface. In this case, the Clerouin model can be used to quantify the value of the kinematic viscosity for mixtures of various proportions. This is shown in Figure 5 as a function of the fraction of the high-density CH(Br) material. Curves are shown for discrete times of 5, 10, 15, and 20 ns. Little difference is seen as a function of time, with a relatively low viscosity for the pure low-density material (CH(Br) fraction = 0) and a value approximately 3-4 times higher for the pure high-density material (CH(Br) fraction = 1). All curves show a minimum at a CH(Br) fraction of 25-30%.

B. Plasma binary mass diffusivity

An additional transport term that can strongly affect the flow development is the binary mass diffusivity. Mass diffusivity, as will be shown, affects the growth rate dispersion relation of perturbations on the unstable interface, eventually causing stability at sufficiently large wavenumber. For the range of plasma coupling conditions of interest ($\Gamma \sim 1$), the method of Paquette et al. [27] can be used. In this method, the diffusion coefficients are obtained as high-accuracy analytic fits to numerically evaluated collision integrals for a screened Coulomb potential. By contrast with the method of Clerouin used for estimating plasma viscosity, the method of Paquette is rigorously valid in the dilute plasma regime and is extrapolated to the dense plasma regime. Again, by comparison with molecular dynamics simulations in the dense plasma regime, the method is shown to provide reasonable estimates in the intermediate region ($\Gamma \sim 1$) of interest to the present experiments.

Figure 6(a) shows a plot of the binary mass diffusivity D_{12} at the interface as a function of time. After passage of the shock, D_{12} remains reasonably constant at approximately $0.08 \text{ cm}^2/\text{s}$. The numerical values are observed to be quite close to those of the kinematic viscosity, falling between the values of ν on either side of the interface. The Schmidt number, $Sc = \nu_{\text{avg}} / D_{12}$, quantifying this comparison between diffusion of momentum and mass is plotted in Figure 6(b). Since the kinematic viscosity varies with the mixture proportion as shown in Figure 5, the Schmidt number is plotted in Figure 6(b) based on the pure materials on either side of the interface as well as the average. Prior to shock arrival, the Schmidt number is very large as the materials are in the solid state. After the shock, however, Sc is observed to be of order one, which is characteristic of a wide range of gasses and plasmas. As Figure 6(b) shows, this experiment while being complicated somewhat by a non-constant acceleration and the effects of decompression does have the nice feature of providing reasonably constant transport properties characterized by ν , D_{12} , and Sc .

IV. GROWTH RATE DISPERSION RELATION OF RT AND RM INSTABILITY WITH VISCOSITY AND MASS DIFFUSION

A. The effects of viscosity and mass diffusion on the RT dispersion relation

Having estimated values of both the kinematic viscosity and the mass diffusivity, we can now quantitatively examine their effect on the Rayleigh-Taylor growth rate dispersion relation for this experiment. Even though, as noticed in Figure 3 and discussed in [19], the growth of the initially imposed perturbations quickly enters the non-linear regime, we will focus on quantifying the dispersion relation in the linear regime. This is reasonable, as the emphasis of this paper is on understanding the effect of viscosity and mass diffusion at smaller spatial scales than those originally imposed on the interface. Even though these short wavelength modes originate from a non-linear interaction between longer wavelength modes, their growth (once the driving modes have saturated [22]) will be well described by the linear theory.

An analytical form of the RT dispersion relation including viscous and mass diffusion was given by Duff, Harlow, and Hirt (DHH) [28]. The growth rate $\dot{\eta}(k, t)$ is given by

$$\dot{\eta} = \sqrt{\frac{A k g(t)}{\psi(D, k, t)} + \nu^2 k^4} - (\nu + D_{12}) k^2 \quad (5)$$

where $\psi(D, k, t)$ is the growth rate reduction factor for an interfacial perturbation of wavenumber k due to a temporally increasing diffusional layer thickness $\delta_D = 2\sqrt{D_{12} t}$ of the interface. In DHH, this effect of a growing diffusional layer thickness is referred to as the dynamic diffusion effect, as opposed to the static effect represented by the last term in eqn. (5), which has no explicit time dependence.

$\psi(D, k, t)$ is determined as the eigenvalue of the equation for the velocity perturbation $w(z)$ at the interface (w and z are in the direction normal to the mean interface):

$$\frac{d}{dz} \left(\rho \frac{dw}{dz} \right) = w k^2 \left(\rho - \frac{\psi}{A k} \frac{d\rho}{dz} \right) \quad (6)$$

Equation 6 is solved using a shooting method for a generic density profile given by $\rho = \text{erf}(z/\delta_D)$. Figure 7 shows a plot of $\psi(k, t)$ for $t = 3$ ns (solid line), 8 ns (long dashed line), and 20 ns (short dashed line). The wavenumber range plotted corresponds to wavelengths from 0.5 – 100 μm , fully covering the range wavelengths considered in any of experiments as seen in Tables 1 and 2.

The effect of a time-dependent diffusion at the interface is to produce a finite density gradient, which increases in time throughout the experiment. The reduction in the RT growth rate due solely to this density gradient scale length effect (i.e. ignoring for the time being the effects of viscosity and static mass diffusion) is shown in Figure 8(a) by plotting $\dot{\eta} = \sqrt{A k g(t)/\Psi(k, t)}$ as a function of time and wavenumber. These are shown relative to the classical growth rate $\dot{\eta} = \sqrt{A k g(t)}$ (dotted line), which is normalized to one at $\lambda = 0.5$ μm ($k = 12.56$ rad/ μm). The thickness of the diffusion layer $\delta_D = 2\sqrt{D_{12} t}$ increases from 0.31 to 0.5 to 0.8 μm as time increases from 3 to 8 to 20 ns. The effects of finite interface thickness should be felt when the perturbation wavelength is comparable to the layer thickness, i.e. when $k \delta_D(t) \approx 1$. This corresponds to wavenumbers of 3.2, 2, and 1.25 rad/ μm , respectively. The normalized growth rates shown in Figure 8(a) show a clear departure from the classical value at each of these time-dependent values. The corresponding wavelengths at which $k \delta_D(t) \approx 1$ are 2.0, 3.1, and 5.0 μm , respectively. This spatial scale is smaller than any of the length scales arising due to non-linearity in the perturbation spectra shown in Figure 3. The eight-mode case produced the largest range of shorter wavelength components, but as seen in Table 1 these are all at least a factor of two larger than the diffusion layer thickness even at late time in the experiment.

Note that for large k , the normalized growth rate approaches a constant value. This is consistent with other representations of the effect of a finite density gradient as given for example in [29, 30], where the reduced growth is expressed as $\dot{\eta} = \sqrt{A k g(t)/(1 + k L_\rho)}$,

where L_ρ is a density gradient scale length. For $k \rightarrow \infty$, this expression becomes independent of the wavenumber, consistent with the large k behavior in Figure 8(a).

The effect of viscosity and mass diffusion in eqn. (5) can now be evaluated. For the present experiment, the values of ν and D_{12} to be used in eqn. (5) are reasonably constant in time, but the driving acceleration $g(t)$ as shown in Figure 2(a) varies considerably. Figure 8(b) isolates the effect of viscosity and mass diffusion on the RT growth rate dispersion curves at $t = 3, 8,$ and 20 ns. Note that Ψ is set to one in these plots, so there is no effect of a finite density gradient at the interface in Figure 8(b). These plots are again shown relative to the inviscid growth rate $\dot{\eta} = \sqrt{A k g(t)}$ (dotted line). Two curves are plotted at each time using the kinematic viscosity values on either side of the interface. The solid line in each case corresponds to the high-density side of the interface, and the dashed line gives the dispersion relation on the low-density side of the interface. As was noted in Figure 5, the minimum viscosity actually occurs at a mixture value in between these two extremes. For the present experiment, this minimum is not far from the low-density value, however. For any particular value of k , the growth rate difference due to the viscosity values on either side of the interface is small at early times when the interface acceleration is large. At later times and for large k , however, the first term in the square root of eqn. (5) becomes small in comparison with the viscous term, and the difference in viscosity on either side of the interface becomes more apparent.

Figure 8(c) combines the effects of a finite density gradient and those of viscosity and mass diffusion by plotting the full RT dispersion relation of eqn. (5). The curves have the same form as those of Figure 8(b), but the combined effect gives a greater reduction from the classical value. A clear maximum growth rate corresponding to a most unstable wavelength is now seen at each time plotted. This maximum occurs at $k_m = 6, 3.4,$ and 2.3 rad/ μm for $t = 3, 8,$ and 20 ns, respectively. It is interesting to compare these values with those obtained by including only the effect of viscosity and ignoring all effects of diffusion

(both static and dynamic). For this case, Chandrasekhar [31] has given a simple expression for the most unstable wavenumber, $k_m = \frac{1}{2}(Ag/\nu^2)^{1/3}$ (eqn. 5 also reduces to this expression for $D_{12} = 0$). For $t = 3, 8,$ and 20 ns, this expression gives maxima at $k_m = 34.9, 20.1,$ and 14.6 rad/ μm . In each case, the additional effects due to mass diffusion reduce the most unstable wavenumber by a factor of approximately 6. Thus the effects of mass diffusion are clearly non-negligible in this system when one is considering the evolution of short wavelength modes.

It is also interesting to look at the limiting scale at which instability will occur. For $t = 3, 8,$ and 20 ns, eqn. (5) gives $k = 21, 12,$ and 8 rad/ μm as the wavenumbers at which the RT growth rate goes to zero. This corresponds to wavelengths from 0.3 to 0.78 μm . These cutoff values are smaller than any of the modes listed in Tables 1 or 2, so we may conclude that absolute stabilization will not occur in these experiments. If we focus on the low-wavenumber portion of the dispersion curves ($k < 2$ rad/ μm) as shown in Figure 8(d), however, we see that there is a noticeable growth rate reduction for some of the modes considered in Tables 1 and 2. This reduction, plotted as a fraction of the classical value, is quantified in Tables 3 and 4 for each of these experiments.

Table 3

λ (μm)	$k_{n1} = k_i + k_j$ (rad/ μm)	$\dot{\eta}$ @ 3ns	$\dot{\eta}$ @ 8ns	$\dot{\eta}$ @ 20ns
11.25	0.56	0.96	0.93	0.88
12.00	0.52	0.97	0.94	0.89
12.86	0.49	0.97	0.94	0.89
13.85	0.45	0.97	0.94	0.90
15.00	0.42	0.97	0.95	0.91
16.36	0.38	0.98	0.95	0.92
18.00	0.35	0.98	0.96	0.92
20.00	0.31	0.98	0.96	0.93

Table 4

λ (μm)	$k_{nl} = k_i + k_j$ (rad/ μm)	$\dot{\eta}$ @3ns	$\dot{\eta}$ @8ns	$\dot{\eta}$ @20ns
2.5	2.51	0.87	0.73	0.59
4.55	1.38	0.93	0.84	0.74
5.56	1.13	0.94	0.87	0.78
25	0.25	0.99	0.97	0.94

For the eight-mode experiment, only a rather modest reduction in growth rate is observed for any of the modes generated through the non-linear interaction of the initially imposed modes. Since the initial linear phase growth is exponential, however, this reduction is not negligible. The shortest wavelength mode of $11.25 \mu\text{m}$, for example, will grow to only 88% of the inviscid amplitude by 3 ns. If the amplitude remained in the linear regime to 8 ns, the amplitude resulting in the presence of these dissipative effects would only be 57% of the inviscid value.

The growth reduction in the two-mode experiment of Table 4 is much more significant. By 3 ns, the shortest wavelength mode $\lambda = 2.5 \mu\text{m}$ will grow to an amplitude of 68% of the inviscid value. By 8 ns, the amplitude is only 11%. This level of growth rate reduction will clearly affect the resulting evolution of the perturbation, and it has significant implications for the numerical simulation of the evolution of such short wavelength perturbations using inviscid numerical methods.

B. The effects of viscosity and mass diffusion on the RM dispersion relation

A similar effect is seen for the impulsively driven, Richtmyer-Meshkov phase of the perturbation evolution, which occurs following shock refraction through the interface. In this case, several models are available in the literature to separately account for the effects of a finite density gradient at the interface and the effect of viscosity. The effect of a finite interfacial density gradient was shown by Mikaelian [32] and Brouillette and Sturtevant [33] to affect the growth of an RM unstable perturbation in a very similar manner to that given by DHH for RT instability. Following [33], the reduced growth rate can be written as

$$\dot{\eta}_{RM} = \frac{k \eta_0 A u_c}{\psi(k, D, t)} \quad (7)$$

where $\psi(k, D, t)$ is the same growth rate reduction factor as in eqns (5 & 6). For the conditions of the present experiment, the initial velocity u_c of the contact discontinuity at the interface following shock refraction is 8×10^6 cm/sec. The reduced growth rate of eqn. (7) is plotted in Figure 9(a) at $t = 3, 8,$ and 20 ns using the values of $\psi(k, D, t)$ from Figure 7. The growth rate is shown relative to the classical value for a discontinuous interfacial density profile with $\psi = 1$ (dotted line), which is normalized to one at $k = 12.56$ rad/ μm . The growth rate reduction due to a finite density gradient scale length is seen to be comparable to that for the RT phase of the instability shown in Figure 8(a). Again, the normalized growth rate approaches a constant at large wavenumber.

The effect of viscosity on the RM instability has been considered by several researchers. In ref. [34], the effect of viscosity was expressed as

$$\dot{\eta}_{Mikaelian} = k \eta_0 A u_c \exp[-2k^2 \nu_{avg} t] \quad (8)$$

where a density-weighted average viscosity across the interface is used. In a more recent study, Carles and Popinet [35] present a different expression for the effect of viscosity on the RM instability derived from an asymptotic analysis of the full Navier-Stokes equations. Their expression is given to first order as

$$\dot{\eta}_{CP} = k \eta_0 A u_c \left[1 - \frac{4}{3\sqrt{\pi}} k \sqrt{\nu_{CP} t} \right] \quad (9)$$

where a somewhat more complicated density-weighted kinematic viscosity is given by

$$\nu_{CP} = \frac{16 (\rho_1 \mu_1) \cdot (\rho_2 \mu_2)}{\left[(\rho_1 + \rho_2) \cdot \left(\sqrt{\rho_1 \mu_1} + \sqrt{\rho_2 \mu_2} \right) \right]^2} \quad (10)$$

The numerical factor of 16 is included so that the average viscosity reduces to the correct limiting values on either side of the interface. Figure 9(b) compares the growth rate reduction given by these two methods. The solid lines give the result of eqn. (9), and the

dashed lines give the reduction of eqn. (8). Again, the inviscid RM growth rate is given by the dotted line. The method of (9) shows a finite wavenumber cutoff due to viscosity, whereas the method of Mikaelian asymptotes to a zero growth rate as $k \rightarrow \infty$. Both methods, however, give reasonably similar magnitudes for the growth rate reduction.

The combined effect of viscosity, mass diffusion, and a finite density gradient scale length has not yet been explicitly discussed in the literature. By comparison with the DHH expression of eqn. (5) for RT instability, however, it seems reasonable to suggest a straightforward combination of the finite density gradient effect of eqn. (7) with the two viscosity models of eqns. (8 & 9). The modified model of Mikaelian thus becomes

$$\dot{\eta}_{Mikaelian} = \frac{k \eta_0 A u_c}{\Psi(k, D, t)} \exp[-2k^2 v_{avg} t] \quad (11)$$

and the model of Carles and Popinet becomes

$$\dot{\eta}_{CP} = \frac{k \eta_0 A u_c}{\Psi(k, D, t)} \left[1 - \frac{4}{3\sqrt{\pi}} k \sqrt{v_{CP} t} \right] \quad (12)$$

The growth rate reduction given by these two modified models is shown in Figure 9(c). As was the case with RT instability, there is now a peak in the growth rate dispersion curves with a corresponding wavenumber of maximum instability. For $t = 3$ ns, the peak growth rate occurs at $k = 6.1$ and 9.0 rad/ μm ($\lambda = 1.0$ and 0.7 μm) for the modified models of eqns. 11 and 12, respectively. At the later times plotted, the peak growth rate occurs at successively smaller wavenumbers.

The wavenumber regime of greatest interest to the present experiments is shown in Figure 9(d) for $0 < k < 2$. In this range, the two models of eqns. (11 & 12) are in excellent agreement. The RM growth rate reduction for the specific wavelength components of interest to the experiments is given in Tables 5 and 6. The reduction is slightly larger than the corresponding values for RT instability, but since the growth rate is initially linear for RM instability, the effect on the perturbation amplitude is not as great as that for RT instability. The shortest wavelength mode of the 8-mode experiment (11.25 μm), for

example, gave a reduced amplitude of 88% by 3 ns from the RT component, whereas for RM instability it is only reduced to 94% of the inviscid value.

Table 5

λ (μm)	$k_{nl} = k_i + k_j$ (rad/ μm)	$\dot{\eta}$ @ 3ns	$\dot{\eta}$ @ 8ns	$\dot{\eta}$ @ 20ns
11.25	0.56	0.94	0.85	0.74
12.00	0.52	0.94	0.86	0.76
12.86	0.49	0.94	0.87	0.77
13.85	0.45	0.95	0.88	0.79
15.00	0.42	0.95	0.89	0.80
16.36	0.38	0.95	0.90	0.82
18.00	0.35	0.95	0.90	0.83
20.00	0.31	0.96	0.91	0.85

Table 6

λ (μm)	$k_{nl} = k_i + k_j$ (rad/ μm)	$\dot{\eta}$ @3ns	$\dot{\eta}$ @8ns	$\dot{\eta}$ @20ns
2.5	2.51	0.75	0.42	0.17
4.55	1.38	0.86	0.66	0.42
5.56	1.13	0.88	0.72	0.51
25	0.25	0.96	0.92	0.87

V. DISCUSSION

The combined effects of viscosity, mass diffusion, and a finite interfacial density gradient have been shown to begin to affect the growth of the RM and RT instabilities in the present experiments at wavelengths of the order of a few microns. Wavelengths considerably shorter than these will be strongly damped, and those considerably longer will behave nearly classically. This has several implications for the present experiments.

First, as stated earlier, these experiments are being performed on the Omega laser to explore the related evolution of RM and RT instabilities in the very similar scaled acceleration history of a supernova. In [36], the Reynolds number characterizing instability

evolution in a supernova was estimated as $Re \sim 10^{10}$, implying a very large separation between the dominant unstable wavelength of interest and the scale on which viscous dissipation will occur. Using the characteristic values given in [36] of $g \approx 10^3 \text{ cm/s}^2$, $\lambda \approx 10^{11} \text{ cm}$, and $\nu \approx 10^7 \text{ cm}^2/\text{s}$, and assuming that $D_{12} = \nu$, we can estimate from eqn. (5) the length scale at which RT growth will begin to depart from the classical value. For $\Psi = 1$, eqn. (5) gives a 50% reduction in the RT growth rate for a wavelength of order 10^5 cm , 6 orders of magnitude lower than the dominant length scale of interest. In the laser experiment by comparison, we have at most 2 orders of magnitude between the largest imposed perturbation length scale and that at which the RT growth rate is reduced by a factor of two. The analogy between the scaled experiment and the full-scale supernova will be preserved at the largest wavelengths, but not at smaller scales. In this regard, the increased energy offered by larger lasers such as the National Ignition Facility (NIF) and the Laser Mega Joule (LMJ) will allow for the use of larger targets and a corresponding increase in the range of scales unaffected by small-scale dissipation.

The present analysis is also of importance in the numerical simulation of these experiments. Since radiation-hydrodynamics codes typically used to model these experiments or related ICF implosions considering short wavelength modes [5-12] do not include viscosity or diffusion, they will over-estimate the growth of short wavelength modes giving rise to possibly erroneous results. This is becoming increasingly more important as both experiments and corresponding numerical simulations evolve toward interfacial structure with increasingly more complicated modal content of decreasing spatial scale.

VI. ACKNOWLEDGEMENTS

This work was performed under the auspices of the U.S. Department of Energy by the University of California, Lawrence Livermore National Laboratory under contract No. W-7405-Eng-48.

VII. REFERENCES

- ¹R.D. Richtmyer, *Commun. Pure Appl. Math.* **13**, 297 (1960).
- ²E.E. Meshkov, *Izv. Acad. Sci. USSR Fluid Dynamics* **4**, 101 (1969).
- ³Lord Rayleigh, *Scientific Papers II* (Cambridge, England), 200 (1900).
- ⁴G.I. Taylor, *Proc. R. Soc. London, Ser. A* **201**, 192 (1950).
- ⁵J. Kane, D. Arnett, B.A. Remington, S.G. Glendinning, J. Castor, R. Wallace, A. Rubenchik, and B.A. Fryxell, *Astrophys. J. Lett.* **478**, L75 (1997).
- ⁶B.A. Remington, J. Kane, R.P. Drake, *et al.*, *Phys. Plasmas* **4**, 1994 (1997).
- ⁷J. Kane, D. Arnett, B.A. Remington, S.G. Glendinning, G. Bazan, R.P. Drake, B.A. Fryxell, R. Teyssier, and K. Moore, *Phys. Plasmas* **6**, 2065 (1999).
- ⁸J. Kane, D. Arnett, B.A. Remington, S.G. Glendinning, G. Bazan, E. Müller, B.A. Fryxell, and R. Teyssier, *Astrophys. J.* **528**, 989 (2000).
- ⁹H.F. Robey, J.O. Kane, B.A. Remington, R.P. Drake, O.A. Hurricane, H. Louis, R.J. Wallace, J. Knauer, P. Keiter, D. Arnett, D.D. Ryutov, *Phys. Plasmas* **8**(5), 2446 (2001)
- ¹⁰P.A. Amendt, J.D. Colvin, J.D. Ramshaw *et al.*, *Phys. Plasmas* **10**(3), 820 (2003).
- ¹¹J.M. Milovich, P.A. Amendt, M.M. Marinak *et al.*, in submission to *Phys. Plasmas* (2003).
- ¹²J.M. Milovich *et al.*, *Proc. IFSA TuPo2.28* (2003).
- ¹³D.D. Ryutov, *Phys. Plasmas Lett.* **7**(12), 4797 (2000).
- ¹⁴J.M. Soures, R.L. McCrory, C.P. Verdon, *et al.*, *Phys. Plasmas* **3**, 2108 (1996).
- ¹⁵T.R. Boehly, D.L. Brown, R.S. Craxton, *et al.*, *Optics-Communications* **133**, 495 (1997).
- ¹⁶D.K. Bradley, J.A. Delettrez, R. Epstein, *et al.*, *Phys. Plasmas* **5**, 1870 (1998).
- ¹⁷M. Brouillette & R. Bonazza, *Phys. Fluids* **11**(5), 1127 (1999).
- ¹⁸J.T. Larsen & S.M. Lane, *J. Quant. Spectrosc. Radiat. Transfer* **51**, 179 (1994).

- ¹⁹H.F. Robey, Y. Zhou, A.C. Buckingham *et al.*, *Phys. Plasmas* **10**, 614 (2003).
- ²⁰K.S. Budil, T.S. Perry, P.M. Bell, J.D. Hares, P.L. Miller, T.A. Peyser, R. Wallace, H. Louis, D.E. Smith, *Rev. Sci. Instrum.* **67**, 485 (1996).
- ²¹S. Haan, *Phys. Rev. A* **39**, 5812 (1989).
- ²²D. Ofer, U. Alon, D. Shvarts *et al.*, *Phys. Plasmas* **3**(8), 3073 (1996).
- ²³A. Miles, J. Edwards, J.A. Greenough *et al.*, submitted to *Phys. Plasmas* (2003).
- ²⁴S.I. Braginski, in Reviews of Plasma Physics, New York, Consultants Bureau (1965).
- ²⁵J.D. Huba, NRL Plasma Formulary, Naval Research Laboratory (1998).
- ²⁶J.G. Clerouin, M.H. Cherfi, and G. Zerah, *Europhys. Lett.* **42**, 37 (1998).
- ²⁷C. Paquette, C. Pelletier, G. Fontaine, and G. Michaud, *Astrophys. J. Suppl. Ser.* **61**, 177 (1986).
- ²⁸R.E. Duff, F.H. Harlow, and C.W. Hirt, *Phys. Fluids* **5**(4), 417 (1962).
- ²⁹H. Takabe, K. Mima, L. Montierth, and R.L. Morse, *Phys. Fluids* **28**, 3676 (1985).
- ³⁰R. Betti, V.N. Goncharov, R.L. McCrory, and C.P. Verdon, *Phys. Plasmas* **5**(5), 1446 (1998).
- ³¹S. Chandrasekhar, “*Hydrodynamic and Hydromagnetic Stability*”, Dover Publications, Inc., New York (1961).
- ³²K. Mikaelian, *Phys. Fluids* **11**(3), 2638 (1991).
- ³³M. Brouillette and B. Sturtevant, *J. Fluid Mech.* **263**, 271 (1994).
- ³⁴K. Mikaelian, *Phys. Rev. E* **47**(1), 375 (1993).
- ³⁵P. Carles and S. Popinet, *Phys. Fluids* **13**(7), 1833 (2001).
- ³⁶D.D. Ryutov, R.P. Drake, J.Kane *et al*, *Astrophys. J.* **518**, 821 (1999).

VIII. FIGURE CAPTIONS

Figure 1. (a) Photograph of typical experimental target. (b) schematic of a two-dimensional slice through the center of the target.

Figure 2. Time history of the (a) the unperturbed interface deceleration, and (b) the Atwood number.

Figure 3. Radiograph of the interface at $t = 13$ ns for and interfacial perturbation with (a) single mode, (b) two-modes (c) eight-modes.

Figure 4. Temporal history of (a) the plasma coupling parameter Γ , and (b) the kinematic viscosity for each of the pure materials on either side of the interface.

Figure 5. Kinematic viscosity for a mixture vs. CHBr fraction

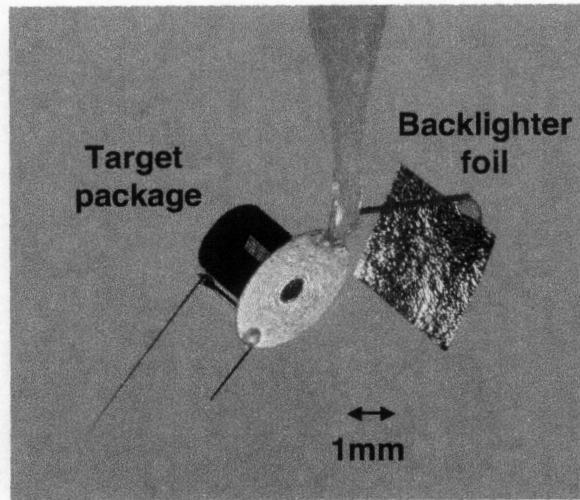
Figure 6. Temporal history of (a) the binary mass diffusivity and (b) the Schmidt number at the interface.

Figure 7. Growth rate reduction factor ψ for $t = 3, 8,$ and 20 ns due to finite density gradient scale length at the interface.

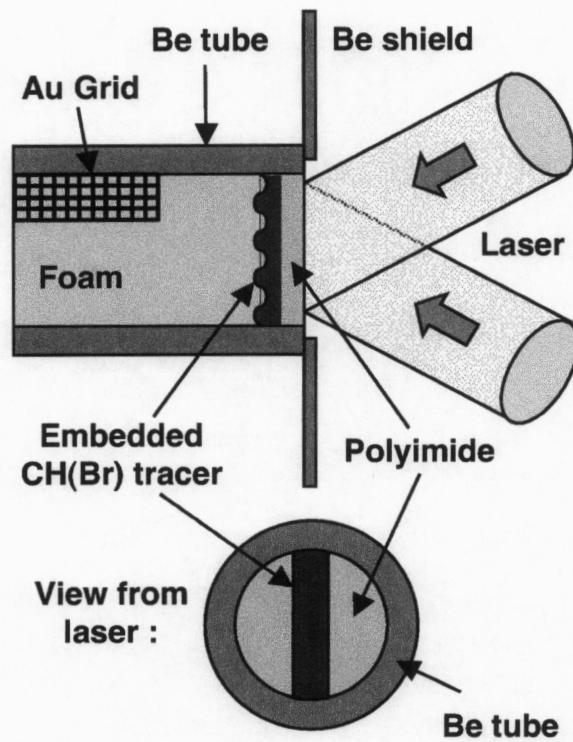
Figure 8. Rayleigh-Taylor growth rate dispersion curve for $t = 3, 10,$ and 20 ns. (a) Effect of a finite density gradient scale length on RT growth rate. (b) Effect of viscosity and mass diffusion on RT growth rate. (c) Effect of viscosity, mass diffusion, and finite density

gradient scale length on RT growth rate. (d) Details of low wavenumber ($0 < k < 2 \text{ rad}/\mu\text{m}$) portion of dispersion curve.

Figure 9. Richtmyer-Meshkov growth rate dispersion curve for $t = 3, 8, \text{ and } 20 \text{ ns}$. (a) Effect of a finite density gradient scale length on RM growth rate. (b) Effect of viscosity and mass diffusion on RM growth rate. (c) Effect of viscosity, mass diffusion, and finite density gradient scale length on RM growth rate. (d) Details of low wavenumber ($0 < k < 2 \text{ rad}/\mu\text{m}$) portion of dispersion curve.

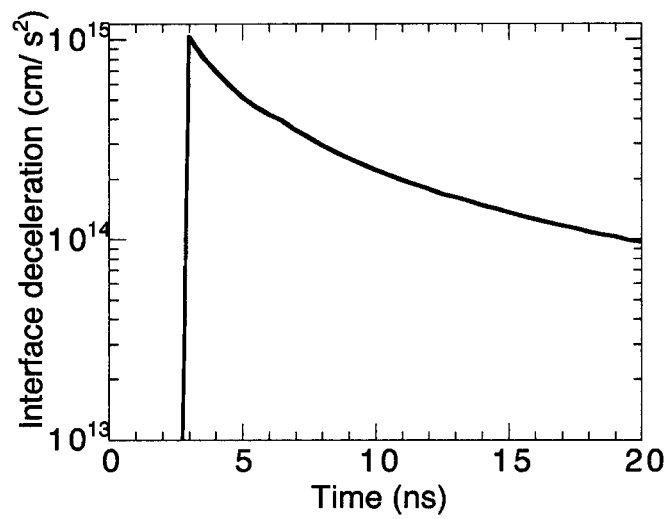


(a)

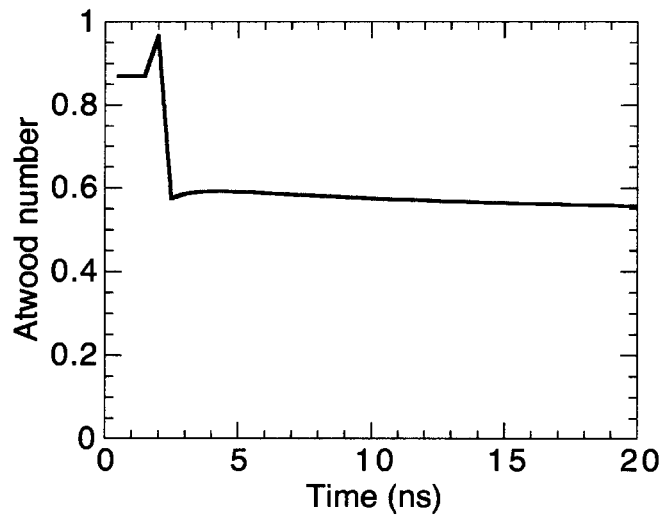


(b)

Figure 1, Robey, Phys. Plasmas

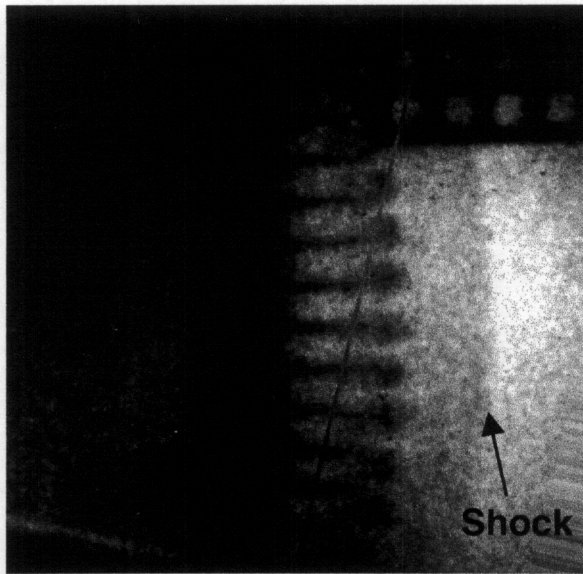


(a)

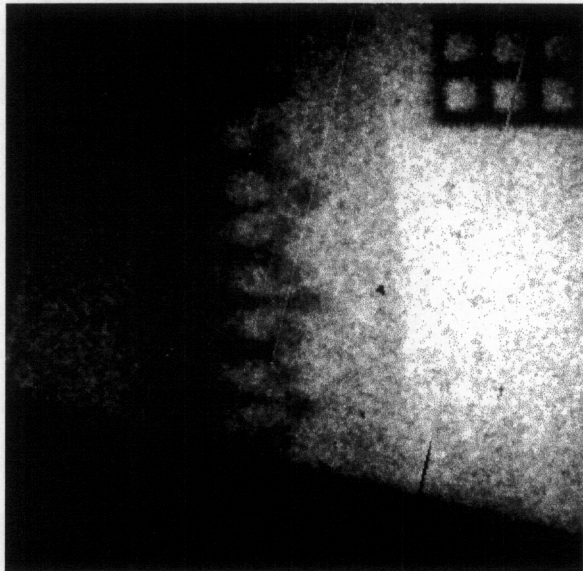


(b)

Figure 2, Robey, Phys. Plasmas



(a)

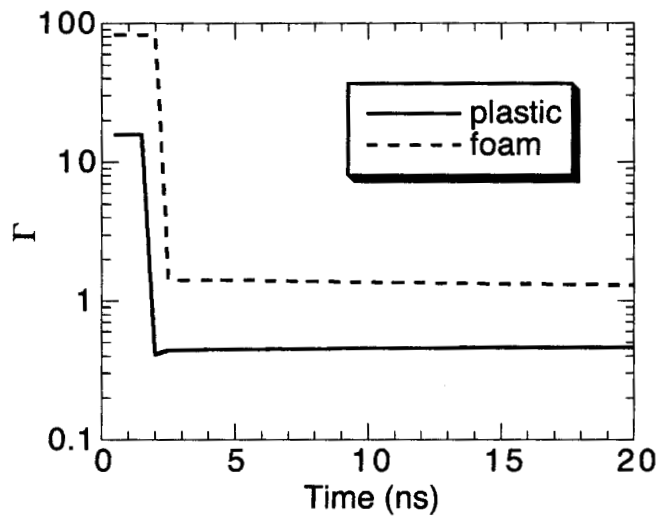


(b)

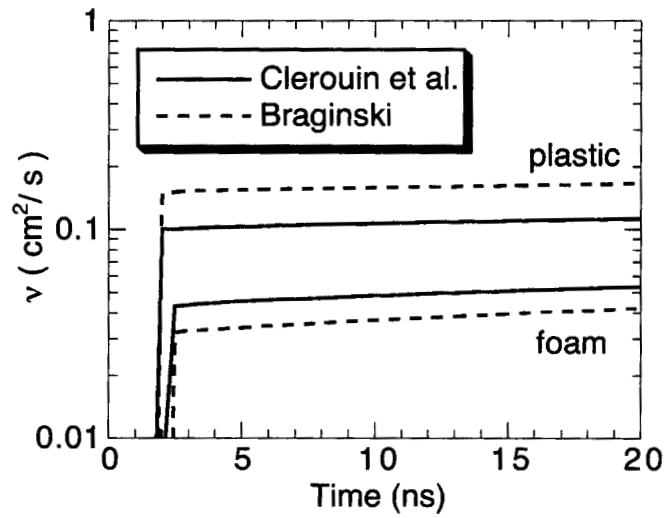


(c)

Figure 3, Robey, Phys. Plasmas



(a)



(b)

Figure 4, Robey, Phys. Plasmas

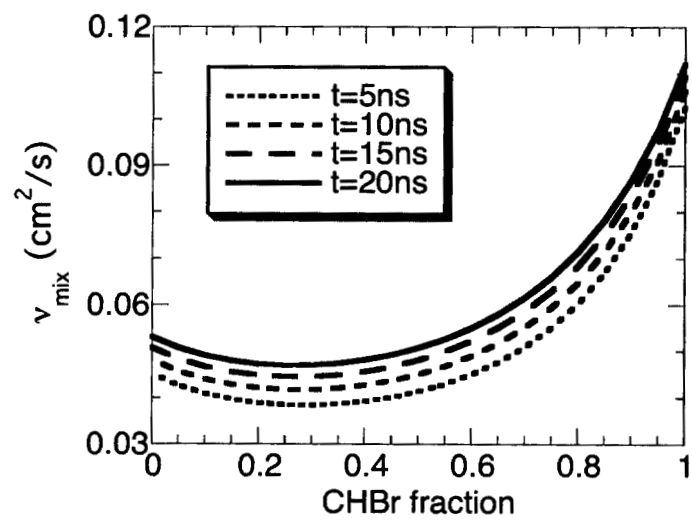
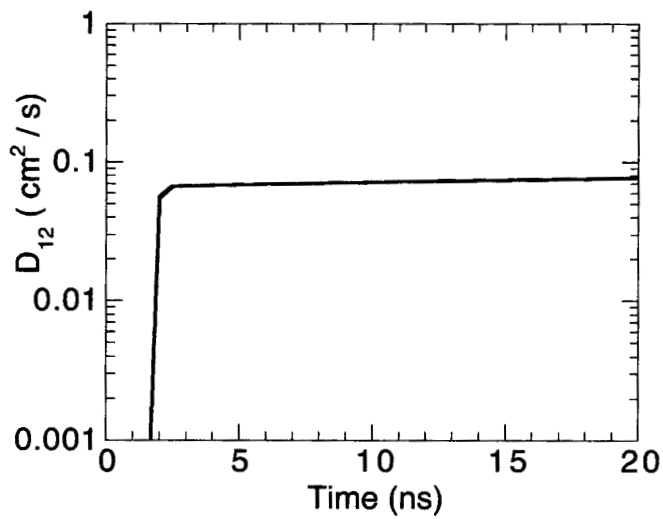
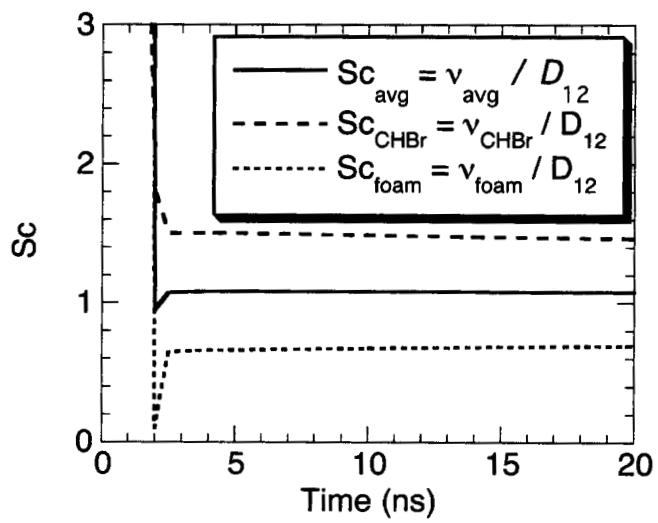


Figure 5, Robey, Phys. Plasmas



(a)



(b)

Figure 6, Robey, Phys. Plasmas

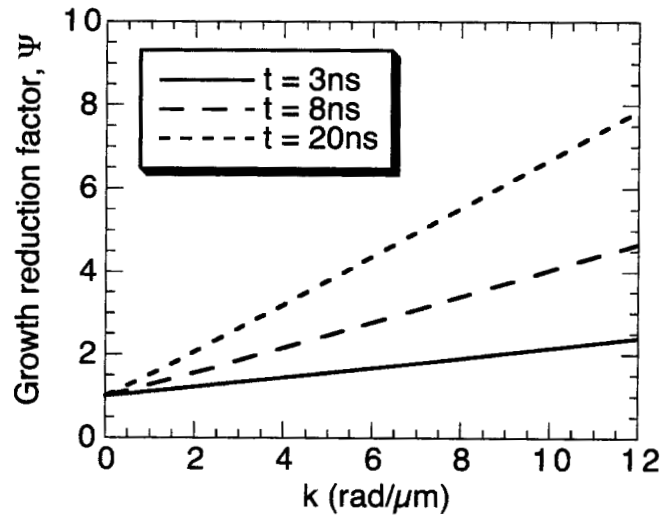
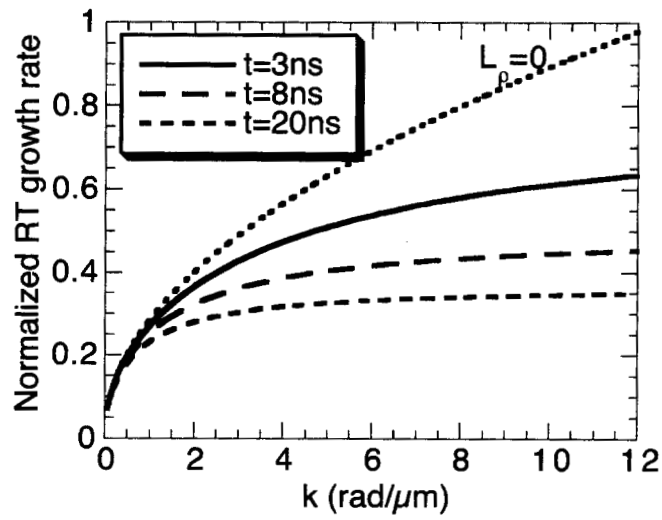
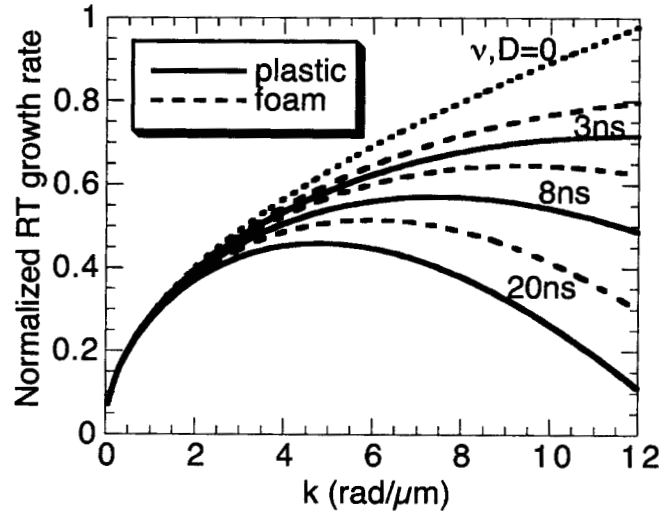


Figure 7, Robey, Phys. Plasmas

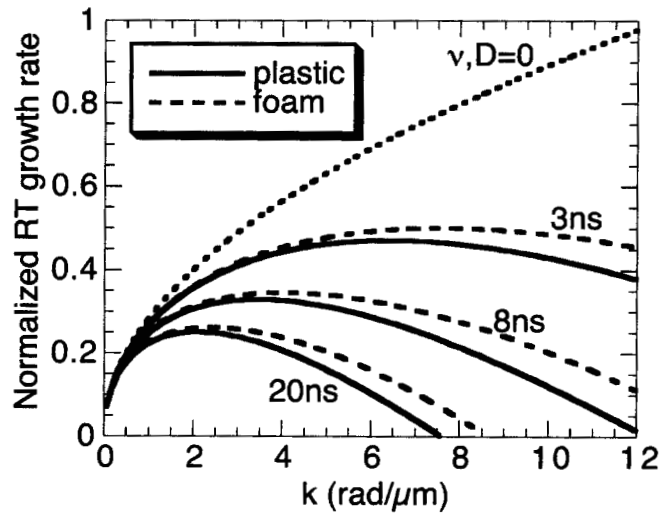


(a)

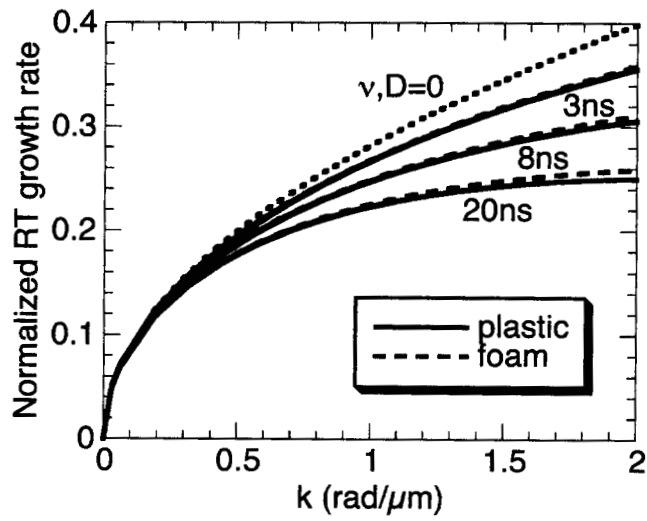


(b)

Figure 8, Robey, Phys. Plasmas

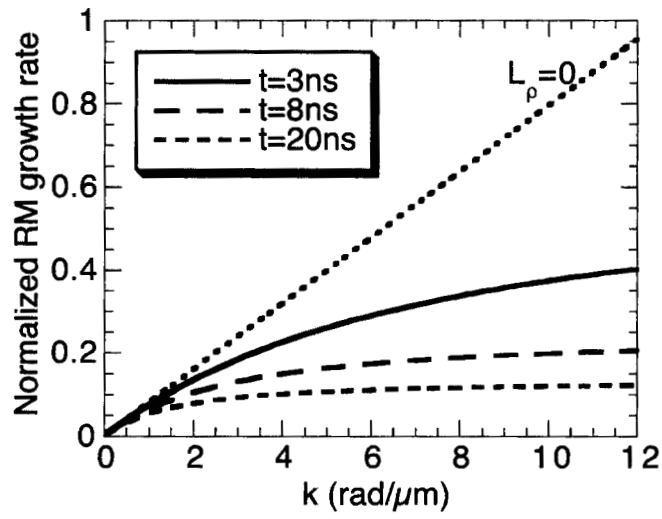


(c)

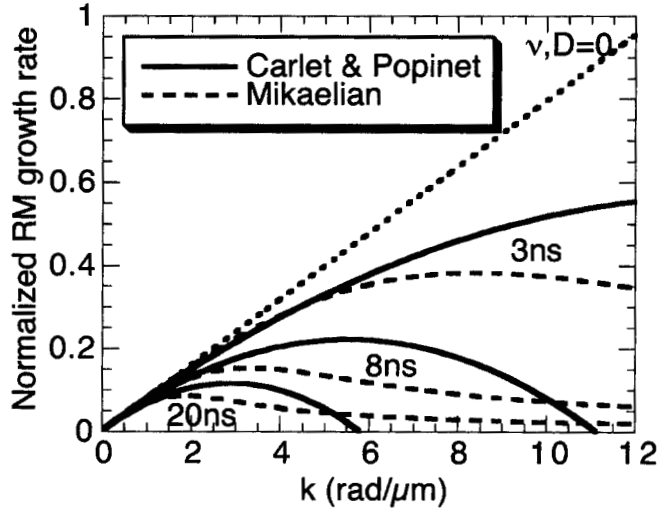


(d)

Figure 8, Robey, Phys. Plasmas

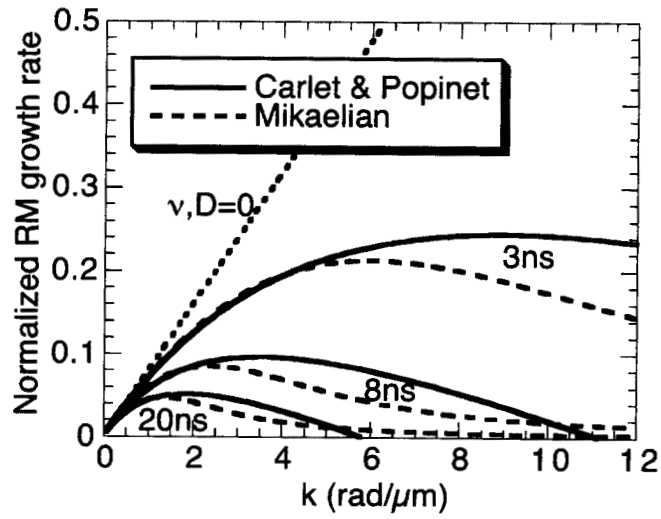


(a)

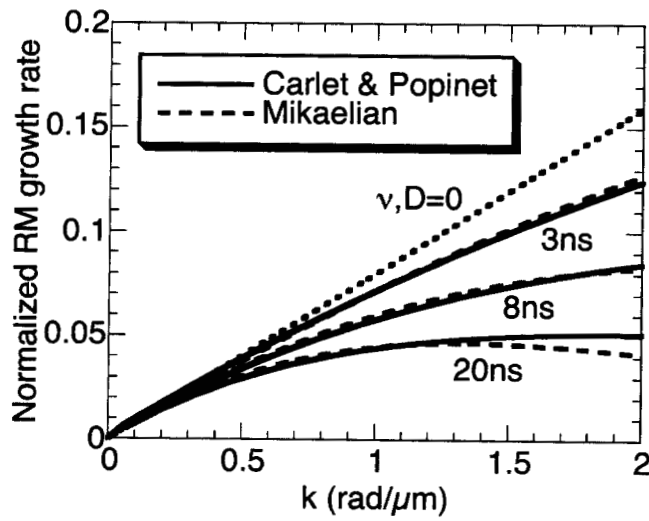


(b)

Figure 9, Robey, Phys. Plasmas



(c)



(d)

Figure 9, Robey, Phys. Plasmas